An optimal penalty method for the joint stiffening in beam models of additively manufactured lattice structures

T. Cadart, T. Hirschler, S. Bahi, S. Roth, F. Demoly, N. Lebaal

International Journal of Solids and Structures 306 (2025) 113107

Contents lists available at ScienceDirect

International Journal of Solids and Structures

journal homepage: www.elsevier.com/locate/ijsolstr

An optimal penalty method for the joint stiffening in beam models of additively manufactured lattice structures

T. Cadart [a,*], T. Hirschler [a], S. Bahi [b], S. Roth [a], F. Demoly [a,c], N. Lebaal [a]

[a] ICB UMR 6303 CNRS, Belfort-Montbéliard University of Technology, UTBM, Belfort, France
[b] Laboratoire d'Études des Microstructures et de Mécanique des Matériaux (LEM3), Université de Lorraine, Metz, France
[c] Institut universitaire de France (IUF), Paris, France

ARTICLE INFO

Keywords:
Lattice structure
Beam formulation
Penalty method
Joint stiffening
Optimization
Additive manufacturing
Material jetting

ABSTRACT

Additive manufacturing is revolutionizing structural design, with lattice structures becoming increasingly prominent due to their superior mechanical properties. However, simulating these structures quickly and accurately using the finite element method (FEM) remains challenging. Recent research has highlighted beam element simulation within FEM as a more efficient alternative to traditional solid FE simulations, achieving similar accuracy with reduced computational resources. However, a significant challenge is managing the lack of rigidity at nodes and the prevalence of low aspect ratio beams. While various methodologies have been proposed to address these issues, there is still a gap in the comprehensive evaluation of their limitations. An optimal node penalization methodology is required to expand the limited range of accurately represented lattice behavior. A preliminary study investigates lattice geometries through comparative analysis of solid and beam FE simulations. Built on this, we developed a methodology suitable to linear, dynamics and nonlinear beam FE simulations, contributing to enhanced computational speed and accuracy. Several lattice structures were printed using material jetting and quasi-static compressive tests were conducted to validate the methodology's accuracy. The numerical results reveal a good accuracy between the proposed beam FE methodology and the experimental data, offering a better alternative to conventional FEM for energy absorption in terms of computing time.

1. Introduction

In recent years, additive manufacturing (AM) has opened doors to innovative structures with unique mechanical properties (Wu et al., 2023; Helou and Kara, 2018; Dadashi and Rahimi, 2024). Of particular interest are lattice structures, which offer various functionalities, such as energy absorption (Yin et al., 2023; Zhang et al., 2024; Hajjari et al., 2021) and vibration damping (Zheng et al., 2023; Lumpe and Stankovic, 2021), making them applicable across various industries including automotive, aerospace, and sports equipment to name a few. However, exploring the design space of lattice structures poses significant computational challenges (Zheng et al., 2023; Lumpe and Stankovic, 2021). Therefore, developing accurate and efficient simulation methods is crucial. Standard solid or volumetric finite element (FE) models require high computational costs due to the intricate three-dimensional mesh of lattice structures. To mitigate this, two main strategies have emerged.

On the one hand, multiscale homogenization methods have been developed to simulate the mechanical behavior of heterogeneous structures across multiple scales (Somnic and Jo, 2022b; Glaesener et al., 2019). These approaches compute an equivalent macroscale behavior from analyses occurring in the underlying heterogeneous microstructure (often denoted as the Representative Volume Element or the Unit Cell in the context of periodic metamaterials). For instance, multilevel FEM (FE2 Glaesener et al., 2021; Raju et al., 2021; Monaldo and Marfia, 2021), computes homogenized fields from the unit-cell FE model and assigns them at each integration point of the macroscale FE model; the Multiscale FEM (MsFEM Wang et al., 2023; Henyš et al., 2019; Zhang et al., 2010) where numerically computed basis functions that encode the microscale heterogeneity; or direct (eventually high-order) numerical homogenization (Somnic and Jo, 2022a; Glaesener et al., 2020; Arabnejad and Pasini, 2013; Hassani and Hinton, 1998) where macroscale material parameters are identified from several analyses performed over the microscale model. Nowadays, in this context of multiscale homogenization, it is a common practice to use the microscale models to train surrogate models which are then used later on during the macroscale simulations to reduce the overall computational time (polynomial function Costa et al., 2022, kriging Liu et al., 2022,

* Corresponding author.
E-mail addresses: thomas.cadart@utbm.fr (T. Cadart), nadhir.lebaal@utbm.fr (N. Lebaal).

https://doi.org/10.1016/j.ijsolstr.2024.113107
Received 8 May 2024; Received in revised form 5 September 2024; Accepted 11 October 2024
Available online 16 October 2024

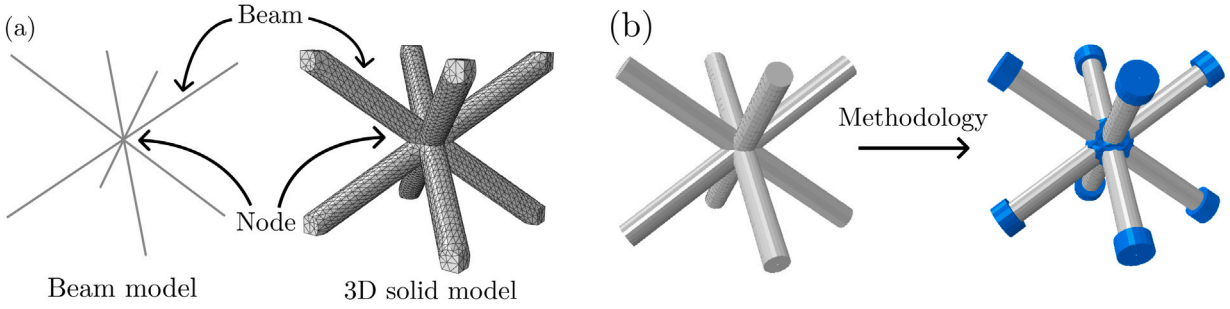

Fig. 1. (a) Comparison of node dimensions according to the beam model and the 3D model for the Body Centered Cubic unit cell (BCC) (b) Methodology applied to the BCC unit cell.

neural network Ross and Hambleton, 2021; Gao et al., 2023; Dos Reis and Karathanasopoulos, 2022). However, their effectiveness relies on a clear separation of scales, which may not always hold true for lattice structures due to minimal available length scales imposed by AM techniques.

On the other hand, full-scale modeling approaches leverage advanced models and numerical methods to solve fine-scale problems efficiently (Hirschler et al., 2022, 2024). For truss-based lattice structures, employing beam formulations can significantly reduce computational costs (Weeger et al., 2023; Musenich et al., 2023). However, standard beam models may overlook material concentration at junctions within lattice structures (see Fig. 1(a)), which leads to underestimate the stiffness of the overall structure (Luxner et al., 2005; Gümrük and Mines, 2013; Smith et al., 2013; Labeas and Sunaric, 2010; Guo et al., 2020; Tahmasebimoradi et al., 2021). To address this limitation, several strategies have been proposed to modify the stiffness at the junctions (Luxner et al., 2005; Gümrük and Mines, 2013; Smith et al., 2013; Labeas and Sunaric, 2010; Guo et al., 2020; Tahmasebimoradi et al., 2021; Terriault and Brailovski, 2018; McDonnell et al., 2024). These modifications are commonly done through two main penalty parameters: the length of the nodal zone denoted in this work l_{zone} , and a second parameter that increases the stiffness within this nodal zone (see Fig. 1(b)). This stiffness increase can either be done by enlarging the cross-sections via a penalty coefficient denoted here α_{r} (*e.g.* in case of circular cross-section defining $R_{zone} = \alpha_{\text{r}} R$), or by increasing the Young's modulus via a penalty parameter denoted here α_E (*i.e.*, defining $E_{zone} = \alpha_E E$).

However, it seems that there is no consensus on the most appropriate penalty parameters for beam models of lattice structures. For example, Luxner et al. (2005) found appropriate results using $\alpha_E = 1000$ to joints with at least four connecting beams, while Gümrük and Mines (2013) recommended $\alpha_E = 1.5$ and $l_{\text{zone}} = R$ for body-centered cubic (BCC) microstructures. Alaimo et al. (2023) optimized the length parameter l_{zone} using a multi-objective genetic algorithm for a BCC lattice structure. Schwahofer et al. (2023) proposed a method to evaluate α_E based on geometric arrangements. Regarding the studies that penalize cross-section dimensions, it appears that setting the penalty coefficient as $\alpha_{\text{r}} = 1.4$ is frequently adopted, see for instance (Smith et al., 2013; Labeas and Sunaric, 2010; Guo et al., 2020; Tahmasebimoradi et al., 2021; Lozanovski et al., 2020b; McDonnell et al., 2024). However, the penalty region l_{zone} varies across these studies. For instance, Smith et al. (2013) and Labeas and Sunaric (2010) select one-tenth of the length of the trusses for lattice geometries such as BCC, BCCZ or F2FCCZ (Face Centered Cubic with beam on Z axis). Guo et al. (2020) employ a more general approach allowing the use of denser lattice structures. They defined l_{zone} by trimming a 3D geometric model at the node. Additionally, let us mention Meng et al. (2020) that employed tapered beams to consider both material accumulation at the truss junctions and other geometric defects coming from AM. Weeger et al. (2019) utilized a more sophisticated method: defining the radius by a quadratic B-Spline curve which leads to smooth and regular cross-section variations. Finally, Tahmasebimoradi et al. (2021) introduced a hybrid method using solid elements over the joint regions and beam elements elsewhere.

While these methods focus on specific lattice geometries within narrow relative density (*i.e.*, the ratio between the amount of material and the volume enclosing the unit cell) ranges, several studies introduce advanced models which incorporate material or geometric non-linearities (Guo et al., 2020; Weeger et al., 2023; Tahmasebimoradi et al., 2021; Meng et al., 2020; Lozanovski et al., 2020b; Gärtner et al., 2021; Lozanovski et al., 2020a; Smith et al., 2013). This diversity complicates reproducibility and comparability of results, hindering the identification of a generic strategy for a wide range of lattice structures achievable through AM. The dynamic modeling of lattice structures, including damping properties (Liu et al., 2021a; Scalzo et al., 2021) and responses to high-speed impacts (Xiao et al., 2020; Dwyer et al., 2023; Ling et al., 2019; Yang et al., 2023), are also of interest, yet few studies employ beam modeling in such numerical simulations. Scalzo et al. (2021) implemented a beam model with $l_{\text{zone}} = R$ and $\alpha_{\text{r}} = 1.4$, aiming to evaluate the damping properties of BCCZ structures with various levels of relative density. Finally, Liu et al. (2021b) presented a method for analyzing the non-linear frequency response, considering the joint as a spatial nonlinear spring–damper system with bilinear hysteresis. Using beam models for dynamic simulation can also be a suitable alternative to solid models. However, it seems that there is no consensus on the penalty parameters necessary to mitigate for the lack of rigidity at the nodes in the context of dynamic analyses too.

Therefore, the objectives of this study are twofold. The first one is to formulate simple static and dynamic problems, along with simple metrics, that enable us to evaluate the accuracy of beam models of lattice structures. Then, using these metrics, the second objective is to identify the optimal penalty parameters of the joint stiffening. Those parameters are investigated by simulating various lattice structures across different relative densities. Finally, once those penalty parameters are in hand, we investigate whether the improvements observed in linear elastic simulations are also observed in more advanced cases, such as elasto-plastic material behavior, geometric non-linearity, or when comparing with experimental data.

This work is organized according to these objectives. Section 2 presents the followed methodology in order to identify the penalty parameters of the joint stiffening. Section 3 presents numerical examples that highlight the performance of the suggested formulation. Finally, in Section 4 we investigate the applicability of the penalty method in more general cases, and Section 5 provides conclusions on the relevance of our methodology for simulating lattice structures with beam models.

2. Beam element penalization methodology

2.1. Beam model accuracy for lattice structures

2.1.1. Beam formulation

In this work, we consider shear-deformable, Timoshenko-like 3D beam models. Let us recall the basics of such a beam formulation in

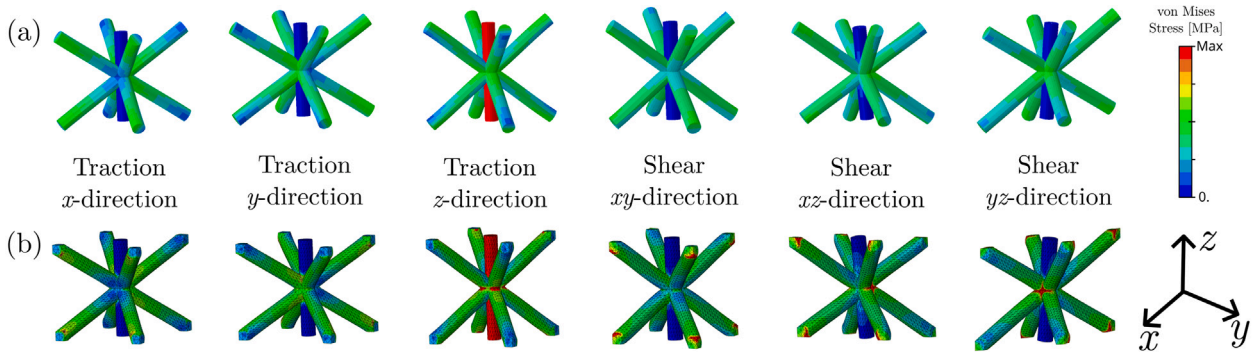

Fig. 2. von Mises stress related to the six loading cases for the BCCZ cell: (a) beam element model, and (b) 3D solid element model.

the context of linear elasticity. The initial configuration of the beam is represented by an arc-length parameterized centerline curve $\boldsymbol{x}_c : [0,l] \to \mathbb{R}^3$ and an orthonormal frame field $\boldsymbol{R} : [0,l] \to \mathrm{SO}(3)$ describing the cross-section orientation. The map from the initial configuration to the deformed configuration is described by the displacement field of the centerline $\boldsymbol{u}_c : [0,l] \to \mathbb{R}^3$ and the cross-section rotational field $\boldsymbol{\theta} : [0,l] \to \mathbb{R}^3$. More specifically, the strain measures, according to the Timoshenko beam theory, can be expressed as follows:

$$\boldsymbol{\epsilon} = \begin{pmatrix} e_t \\ \gamma_1 \\ \gamma_2 \end{pmatrix} = \boldsymbol{R}^\top \boldsymbol{u}_c' + \boldsymbol{e}_1 \times \boldsymbol{\theta}, \qquad \boldsymbol{\kappa} = \begin{pmatrix} \kappa_t \\ \kappa_1 \\ \kappa_2 \end{pmatrix} = \boldsymbol{\theta}', \tag{1}$$

where $(\cdot)'$ denotes the arc-length derivative, $\boldsymbol{e}_1$ the first Cartesian vector, $\boldsymbol{\epsilon}$ the tensile and shear strain vector, and $\boldsymbol{\kappa}$ the torsional and bending strain vector.

For an isotropic elastic material, the constitutive relation can be characterized by a Young's modulus E and a shear modulus G. The internal forces $\boldsymbol{n}$ and moments $\boldsymbol{m}$ are then given by:

$$\boldsymbol{n} = \boldsymbol{A}\boldsymbol{\epsilon}, \quad \boldsymbol{A} = \mathrm{diag}\begin{pmatrix} EA & GA_1 & GA_2 \end{pmatrix}, \tag{2}$$

$$\boldsymbol{m} = \boldsymbol{B}\boldsymbol{\kappa}, \quad \boldsymbol{B} = \mathrm{diag}\begin{pmatrix} GJ & EI_1 & EI_2 \end{pmatrix}, \tag{3}$$

where A, A_1, and A_2 defines the cross-section area and shear areas, respectively, and J, I_1, and I_2 defines the torsional constant and second moments of area, respectively. Shear and torsion are often scaled with correction factors, *i.e.*, in general $A_i \neq A$ and $J \neq I_1 + I_2$. Readers may refer to Pilkey (2002) for more details regarding Timoshenko-like beam models.

Finally, we recall the variational formulations associated with such a beam model. The static equilibrium of a structure modeled with Timoshenko beams may involve weak problems of the following form:

$$\int_{[0,l]} \boldsymbol{n} \cdot \delta\boldsymbol{\epsilon} + \boldsymbol{m} \cdot \delta\boldsymbol{\kappa} \, \mathrm{dl} = \int_{[0,l]} \boldsymbol{b}_c \cdot \delta\boldsymbol{u} \, \mathrm{dl} + \mathrm{BCs}, \tag{4}$$

where $\boldsymbol{b}_c$ denotes line loads applied along the beam centerline, and BCs denotes additional terms associated with the imposed boundary conditions (e.g., an imposed displacement, an imposed rotation, an applied force, or an applied moment).

2.1.2. Assessment of the beam models accuracy via linear static analyses over representative unit cells

We seek a straightforward method to assess beam models accuracy in the context of lattice structures. The developed approach uses common practices in the context of multi-scale homogenization. The idea is to formulate problems within representative unit cells and subsequently computing several quantities of interests in order to evaluate the accuracy of the model later on. The results obtained with the beam models are compared with those obtained with a solid model.

More specifically, let us define a macro-displacement field $\boldsymbol{u}_0$ over an elementary volume Ω_0 by:

$$\boldsymbol{u}_0(\boldsymbol{x}) = \nabla\hat{\boldsymbol{u}}_0 \cdot \boldsymbol{x}, \quad \text{for } \boldsymbol{x} \in \Omega_0, \tag{5}$$

where the macro-displacement gradient $\nabla\hat{\boldsymbol{u}}_0$ is taken constant over the macro-domain. We are then looking for the fluctuation vector fields, solutions of:

$$\int_\Omega \boldsymbol{\sigma} : \delta\boldsymbol{\epsilon} \, \mathrm{dv} = -\int_\Omega (\boldsymbol{C} : \boldsymbol{\epsilon}(\boldsymbol{u}_0)) : \delta\boldsymbol{\epsilon} \, \mathrm{dv} + \mathrm{PBCs}, \qquad \text{(solid formulation)} \tag{6a}$$

$$\int_{[0,l]} \boldsymbol{n} \cdot \delta\boldsymbol{\epsilon} + \boldsymbol{m} \cdot \delta\boldsymbol{\kappa} \, \mathrm{dl} = -\int_{[0,l]} (\boldsymbol{A}\boldsymbol{\epsilon}(\boldsymbol{u}_0, \boldsymbol{0})) \cdot \delta\boldsymbol{\epsilon} \, \mathrm{dl} + \mathrm{PBCs}, \qquad \text{(beam formulation)} \tag{6b}$$

where, in Eq. (6a), $\boldsymbol{\sigma}$ denotes the linearized Cauchy stress tensor, $\boldsymbol{\epsilon}$ the linearized Green–Lagrange strain tensor, and $\boldsymbol{C}$ the Hooke material tensor. The problems defined in Eq. (6) are solved under periodic boundary conditions (PBCs) which is known, in the context of homogenization, to make the micro-macro-transition fulfill the Hill–Mandel condition. These PBCs can be enforced via multiple point constraints in the case of matching meshes at the periodic interfaces (Omairey et al., 2019). Other more advanced approaches, as for instance the Nitche method, might be used to enforce those PBC for general non-conforming meshes (Henyš et al., 2019). Once the solution of Eq. (6) in hand, one can compute effective (or average) stresses for the solid model $\hat{\boldsymbol{\sigma}}^{\mathrm{solid}}$ or for the beam model $\hat{\boldsymbol{\sigma}}^{\mathrm{beam}}$ as:

$$\hat{\boldsymbol{\sigma}}^{\mathrm{solid}} = \frac{1}{|\Omega_0|}\int_\Omega \boldsymbol{\sigma} \, \mathrm{dv}, \qquad \hat{\boldsymbol{\sigma}}^{\mathrm{beam}} = \frac{1}{|\Omega_0|}\sum_{i\in\mathcal{B}} \boldsymbol{n}^i \otimes \boldsymbol{x}_c^i, \tag{7}$$

where $\mathcal{B}$ denotes the set of boundary nodes.

Finally, the comparison between the beam models and the solid model involves comparing the effective stresses. Here, this done over six loading cases to account for the unit cell's behavior under normal and shear strains, as depicted in Fig. 2. In other words, we choose in Eq. (5), the macro-displacement gradient, and thus, the input displacement fields as:

$$\nabla\hat{\boldsymbol{u}}_0 = \frac{1}{2}\left(\boldsymbol{e}_k \otimes \boldsymbol{e}_l + \boldsymbol{e}_l \otimes \boldsymbol{e}_k\right) \quad \Rightarrow \quad \boldsymbol{u}_0^{kl}(\boldsymbol{x}) = \frac{1}{2}\left(x_l\boldsymbol{e}_k + x_k\boldsymbol{e}_l\right), \text{ for } \boldsymbol{x} \in \Omega_0, \tag{8}$$

where (k,l) take successively the following pairs of values: $\{11, 22, 33, 12, 13, 23\}$. By collecting the effective stresses for all six load cases, the accuracy of a beam model relative to a reference solid model is evaluated as:

$$\epsilon_{\mathrm{static}} = \frac{\|\mathbf{S}^{\mathrm{solid}} - \mathbf{S}^{\mathrm{beam}}\|_F}{\|\mathbf{S}^{\mathrm{solid}}\|_F}, \tag{9}$$

where $\|\cdot\|_F$ denotes the Frobenius norm, and $\mathbf{S} \in \mathbb{R}^{6\times6}$ stacks the vectorized effective stresses (using Voigt notation for instance) for the six load cases:

$$\mathbf{S} = \begin{bmatrix} \hat{\sigma}_{11}^{11} & \hat{\sigma}_{11}^{22} & \cdots & \hat{\sigma}_{11}^{23} \\ \hat{\sigma}_{22}^{11} & \hat{\sigma}_{22}^{22} & \cdots & \hat{\sigma}_{22}^{23} \\ \vdots & \vdots & \ddots & \vdots \\ \hat{\sigma}_{23}^{11} & \hat{\sigma}_{23}^{22} & \cdots & \hat{\sigma}_{23}^{23} \end{bmatrix}, \tag{10}$$

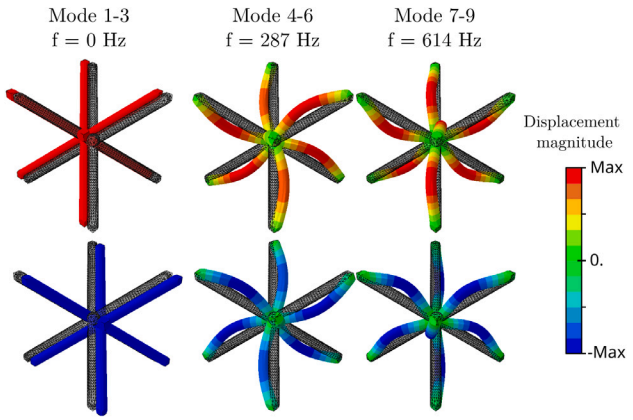

Fig. 3. The first nine vibrational modes of a modal analysis of BCC unit cell, each mode is tripled due to the geometry symmetry.

with $\hat{\sigma}_{ij}^{kl}$ being the ij-component of the effective stresses for the kl-load case. Operator $\boldsymbol{S}$ is the effective elasticity tensor in the context of first-order homogenization. In this study, the computation of the error ϵ_{static} involves evaluating the differences between elasticity tensors obtained from a solid model and a beam model. However, the focus is not directly on effective elasticity tensors. Instead, the error ϵ_{static} is calculated to assess the accuracy of a beam model for a lattice unit cell, offering a relatively quick and general context for evaluation. The Frobenius norm was chosen as the accuracy evaluator due to its simplicity and effectiveness in providing a single, coherent indicator for comparing different models.

2.1.3. Assessment of the beam models accuracy via modal analyses over unit cells

In addition to the static analyses described in Section 2.1.2, it is valuable to compare the dynamic response of lattice structures obtained with beam models to the one obtained with a solid model. To achieve this, natural vibration analyses are performed over representative unit cells, *i.e.*, the solution involves:

$$-\omega^2 \int_{\Omega} \rho \boldsymbol{u} \cdot \delta \boldsymbol{u} \, \mathrm{dv} + \int_{\Omega} \boldsymbol{\sigma} : \delta \boldsymbol{\epsilon} \, \mathrm{dv} = 0 \; + \; \text{PBCs}, \qquad \text{(solid formulation)} \tag{11a}$$

$$-\omega^2 \int_{[0,l]} \mu \boldsymbol{u}_{\mathrm{c}} \cdot \delta \boldsymbol{u}_{\mathrm{c}} \, \mathrm{dl} + \int_{[0,l]} \boldsymbol{n} \cdot \delta \epsilon + \boldsymbol{m} \cdot \delta \boldsymbol{\kappa} \, \mathrm{dl} = 0 \; + \; \text{PBCs}, \qquad \text{(beam formulation)} \tag{11b}$$

where ρ and $\mu = \rho A$ denote the density and the linear density of the material, respectively. In this work, these natural vibration problems are performed under periodic boundary conditions (as for the static analyses, see Eq. (6)). This choice is motivated by the fact that these boundary conditions are often set in the context of (quasi)-periodic media as is the case for lattice structures. Those natural modes could be observed within lattice structures. An example of results is given in Fig. 3.

When performing natural vibration analysis, a fixed number of modes n_{modes} is computed, specifically those associated with the smallest eigenvalues. This is done in this work, and the solid and beam models are compared by computing the following quantity:

$$\epsilon_{\text{dyna}} = \frac{\| \boldsymbol{t}^{\text{solid}} - \boldsymbol{t}^{\text{beam}} \|_2}{\| \boldsymbol{t}^{\text{solid}} \|_2}, \tag{12}$$

where vector $\boldsymbol{t}$ collects the time periods:

$$\boldsymbol{t} = \begin{pmatrix} T_4 & T_5 & \dots & T_{n_{\text{modes}}} \end{pmatrix}, \quad T_i = \frac{2\pi}{\omega_i}. \tag{13}$$

The first three modes are associated with translational rigid body motions (rotational rigid body are removed due to the PBCs), and thus $\omega_1 = \omega_2 = \omega_3 = 0$. We omit those modes that have infinity time periods. We also do not compare the frequencies (or pulsations) directly as it leads to give more importance to the largest computed frequencies. On the contrary, employing the time periods in the expression of ϵ_{dyna} leads to prioritize the smallest computed frequencies.

2.2. Defining the length of the stiffening region

The parameter denoted l_{zone} (the length of the junctions) plays an important role in the numerical simulation, representing the size of the node, and consequently, its rigidity. Four strategies with different definitions of l_{zone}, drawn from the literature and investigated in this work, are detailed below and in Fig. 4:

- Strategy 1: $l_{\text{zone}} = L/10$, with L being the length of the beam as done in Labeas and Sunaric (2010),
- Strategy 2: $l_{\text{zone}} = R$, with R being the radius of the beam according to Gümrük and Mines (2013),
- Strategy 3: $l_{\text{zone}} = R\sqrt{3}$, according to Guo et al. (2020),
- Strategy 4: $l_{\text{zone}}(R, \gamma)$ accounting for joint geometry hereafter.

Among strategies found in the literature, none seems to take into account the arrangement of the beams in the 3D space. However, the angle between the beams influences the overlap at the node, as highlighted in Fig. 5. Indeed, a small angle implies a high nodal overlap. The length l_{zone} can be expressed with respect to the radius R of the beams and the angle γ through the following trigonometric relation:

$$l_{\text{zone}}(R, \gamma) = \frac{R}{\tan(\frac{\gamma}{2})}. \tag{14}$$

The angle γ is formed by the directional vectors of the neutral fibers of two adjacent beams (see Fig. 5 again). In scenarios where more than two beams join at the same node, the smallest angle formed with other beams is considered for each beam. This relationship allows for defining potentially different l_{zone} for each beam along the structure. To simplify the description of the results, each strategy will be referred to by its previously associated number (see Fig. 4).

2.3. Defining the penalty coefficient

Unlike the length of the junctions l_{zone}, it is less straightforward to determine an appropriate value for the parameter that penalizes the structural behavior in these regions. The penalty strategy favored in this work relies on increasing the radius instead of increasing the Young's modulus. This choice was motivated by its widespread use in recent literature (Gümrük and Mines, 2013; Smith et al., 2013; Labeas and Sunaric, 2010; Guo et al., 2020), but the same methodology can be applied if one chooses to penalize the elastic modulus.

The idea is to compute the error ϵ_{static} on various lattice unit cells to identify an appropriate value. More specifically, we consider solving the following optimization problem:

$$\alpha_{\mathrm{r}}^{*} = \underset{\alpha_{\mathrm{r}} \in [1,5]}{\operatorname{argmin}} \; \epsilon_{\text{static}}(\alpha_{\mathrm{r}}), \tag{15}$$

for different unit cells. This optimization problem can be solved with the standard Brent optimization algorithm (Brent and Watson, 1973; Atkinson, 1989). This algorithm was employed in this work due to its straightforward usability and its gradient-free nature.

2.4. Balance the mass distribution

The increase of the cross-sections near the joints compensates for the lack of rigidity at nodes, but it alters the mass distribution within the structure. At every node, the mass is increased due to the penalty coefficient α_{r} that augments the radius of the beam. Even if one chooses to penalize the Young's modulus, the density ρ_{zone} in the nodal zones

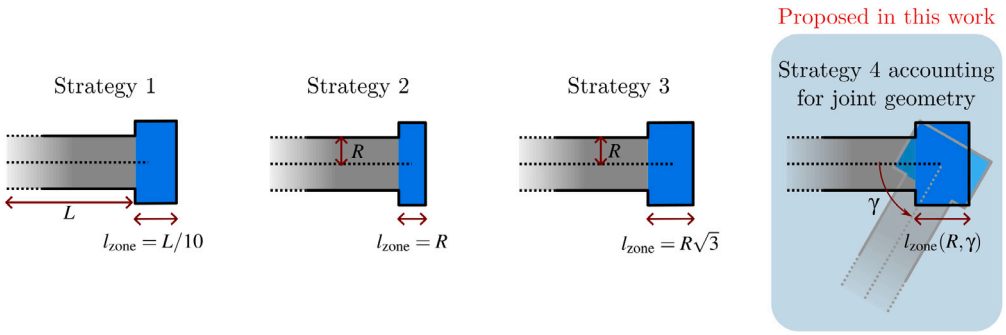

Fig. 4. Comparative schematic of three strategies found in literature (Labeas and Sunaric, 2010; Gümrük and Mines, 2013; Guo et al., 2020) and a novel approach for l_{zone}.

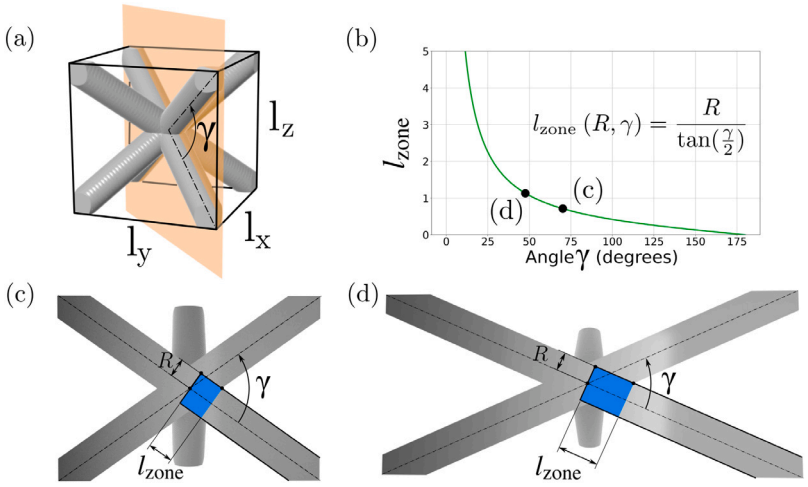

Fig. 5. (a) BCC unit cell half-cut by a center plane (b) Graph illustrating the relationship between l_{zone} and the angle γ with $R = 0.5$ mm (Strategy 4) (c) Cross-sectional view of BCC unit cell ($l_x = l_y = l_z = 5$ mm, $R = 0.5$ mm which implies $\gamma = 70.5°$) (d) Cross-sectional view of BCC ($l_x = l_y = 8$ mm $l_z = 5$ mm, $R = 0.5$ mm which implies $\gamma = 47.7°$).

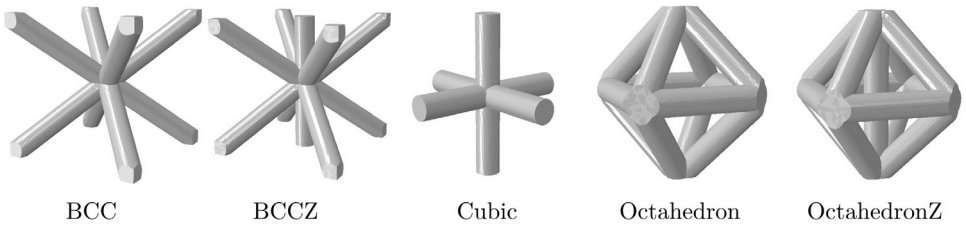

Fig. 6. Set of 3D solid lattice unit cells that are studied in this work.

can also be adapted to compensates for the overlaps near the junctions: beam models usually overestimate the mass of the structures. More precisely, the objective is to define ρ_{zone} so that the mass of the beam model equal an objective mass m_{obj} (which is either the exact mass of the structure obtained with a CAD model or a solid model, or an estimated mass), *i.e.*, we are looking for ρ_{zone} solution of:

$$\int_{\gamma_{int}} \rho A \, \mathrm{dl} + \int_{\gamma_{zone}} \rho_{zone} A_{zone} \, \mathrm{dl} = m_{obj}, \tag{16}$$

where γ_{zone} is the penalized domain and γ_{int} is the internal domain (or the remaining domain), ρ is the material density, and A_{zone} is the area of the cross-sections in the penalized zones. In case of homogeneous material (and thus constant densities), the density ρ_{zone} can be defined as:

$$\rho_{zone} = \frac{1}{V_{zone}}(m_{obj} - \rho V_{int}), \tag{17}$$

where V_{zone} and V_{int} are the volumes of the penalized and internal regions of the beam model, respectively.

3. Numerical examples

Several lattice structure geometries have been chosen, as depicted in Fig. 6, to explore the validity domains of the penalization strategies. Each unit cell has been selected based on its frequent appearance in the literature, such as the Body-Centered Cubic (BCC) cell. The group of unit cells is designed to include structures with a variable number of beams and angles between these beams, aiming to achieve greater diversity within the dataset. All structures were studied in the radius range between 0.025 mm and 0.2 mm, with a step of 0.025 mm. By acting on the radius, the domain of relative density will depend on the structure. This variation is influenced by structural features such as the number of beams and nodes, which determine the material distribution in the cell (Chen et al., 2018a). Beam theory requires a high aspect ratio (beam length/beam radius) to accurately represent mechanical behavior. Thus, the domain is narrowed by calculating the ratio between the smallest beam length in the structure and its radius. For Timoshenko beam model, the limitation of the ratio is set to values

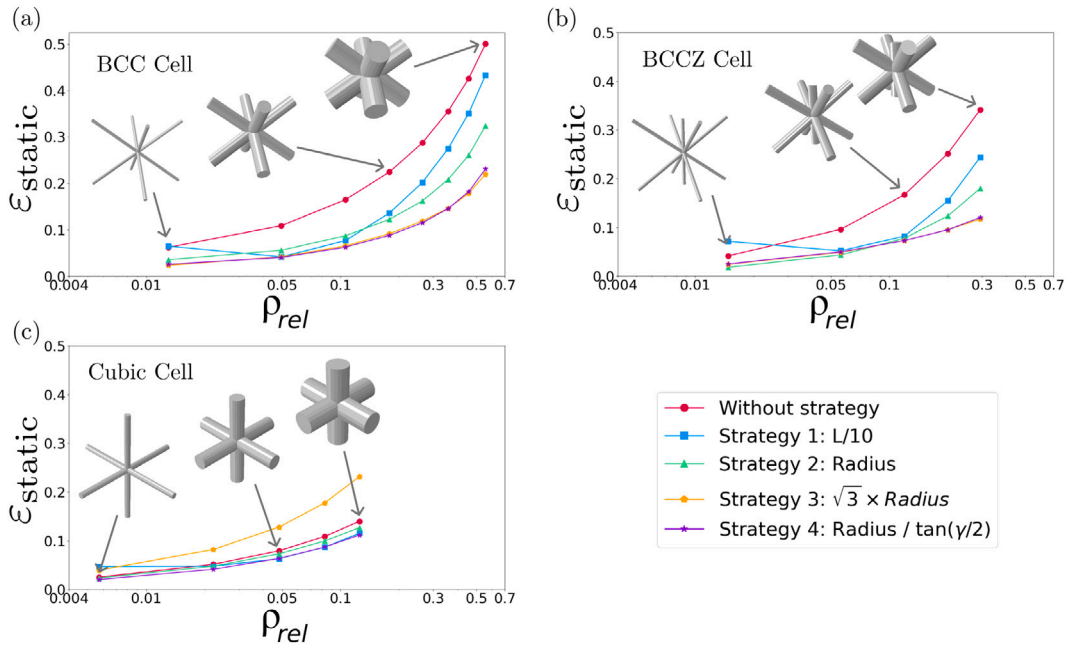

Fig. 7. $\varepsilon_{\text{static}}$ (relative error) as a function of ρ_{rel} (relative density) for multiple modelization strategies for (a) BCC, (b) BCCZ, and (c) Cubic unit cell.

greater than 4 (which already exceeds standard recommendations for these beam elements Schwahofer et al., 2023).

All simulations were conducted with the software Abaqus (Dassault Systèmes, Vélizy-Villacoublay, France, Version 2022) coupled with a Python script allowing rapid modeling, simulation, and extraction of results. Subsequently, after performing a mesh convergence analysis, ten-node tetrahedral elements with an approximate global size of 0.0375 were selected for the 3D solid model. For the beam configuration, Timoshenko beam linear elements sized at 0.2 were adopted.

The material model applied in this section for determining the penalization coefficient is assumed to be purely linear elastic. The Young's modulus, denoted as $E = 1013\,\text{MPa}$, was determined experimentally (further details in Section 4.1). Additional material properties, including a density of $1.18\,\text{g/cm}^3$ and Poisson's ratio of $\nu = 0.3$, were obtained from Stratasys (Ver, 2024).

3.1. Evaluating the effects of l_{zone} the stiffening region on beam model accuracy

To effectively address the stiffness issue in the beam models, a variety of strategies are evaluated in Fig. 7, focusing on three unique geometric configurations. For each strategy, the relative errors are computed within the range of relative density. In this section, the penalty coefficient is set at $\alpha_r = 1.5$. Fig. 7(a) presents the results for the BCC unit cell. For the beam strategy without modification, the relative error rapidly grows as the relative density increases. This highlights the necessity for an approach that considers the concentration of material at the nodes when investigating lattice structures with less slender beams. The results of Strategy 1 are noteworthy as the curve contains a minimum point situated at $\rho_{\text{rel}} = 0.05$. Moreover, at this density, the outcomes are equivalent to both Strategy 3 and Strategy 4. Thus, it becomes evident that Strategy 1 is only efficient with relative densities close to 0.05. While Strategy 2 offers fewer errors than the unmodified approach, Strategies 3 and 4 are the most optimal for this particular cell, yielding comparable results. This can be attributed to the fact that the angle is consistent for all beams in the BCC cell. In this case, Eq. (14) delivers a result close to $R\sqrt{3}$, which corresponds to Strategy 3.

As shown in Fig. 7(b), the various strategies lead to similar results for the BCCZ unit cell than for the BCC cell. It is noteworthy from the analysis that, within the context of low-density ranges, Strategy 2 exhibits enhanced efficacy for the BCCZ cell in comparison to the BCC cell. Strategies 3 and 4 prove once again to be equivalent and highly effective, for the same reasons as mentioned earlier.

In contrast to the previously discussed cells, the Cubic cell is characterized by having fewer beams and exhibiting larger angles between these beams. The analysis of the Cubic cell depicted in Fig. 7(c) shows that Strategy 4 performs the best, whereas Strategy 3 is not as effective compared to its performance in the previous cells. The errors generated by Strategy 3 are more significant than the model without any modification, as it overestimates the length to be modified. In this case, Eq. (14) yields a modification length less than $R\sqrt{3}$. The strategy that consistently delivers stable results across different cell types and relative densities is Strategy 4, as it accounts for both the beam's radius and the angles within the structure. Therefore, our optimal methodology adopts Strategy 4.

3.2. Optimizing the penalty coefficient α_r

Subsequently, the radius increase coefficient α_r was investigated for several cells. Strategy 4, which exhibited the highest performance previously, was selected for the length parameter modification l_{zone}. In Fig. 8, the results indicate that optimizing the penalty parameter (*i.e.*, solving the optimization problem defined in Eq. (15)) diminishes the errors between the solid and beam models throughout the full range of relative densities. This trend is consistently observed across all structural configurations studied.

The optimized coefficients α_r^* of all unit cells and spanning the entire range of studied relative densities, are presented in Fig. 8. The optimal penalty coefficients α_r^* are grouped between 1.3 and 1.63 for all cells. The variations of the parameter across the range of relative density are different depending on the geometry. For instance, α_r^* changes little for the Octahedron cell, while it changes quite significantly for the BCCZ cell. Therefore, it seems not possible to determine a generalized relationship between the stiffening coefficient α_r and relative density ρ_{rel} for all cells. However, as the important thing is to reduce the highest relative errors $\varepsilon_{\text{static}}$, which corresponds to cases of high relative density, it might be relevant to focus on these highest relative densities. The computed average of the optimal coefficients at maximum densities

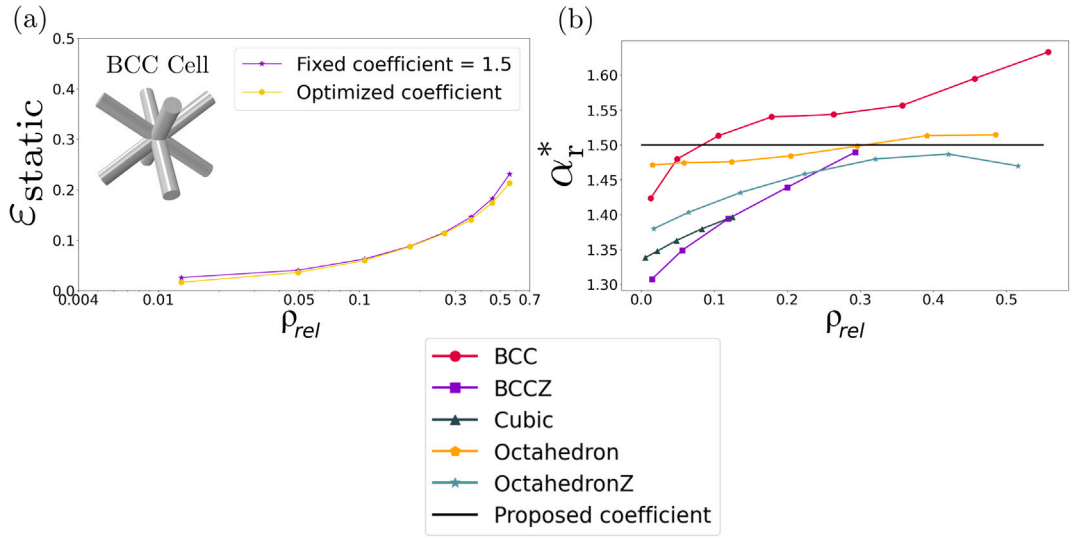

Fig. 8. Optimization result of α_r (a) Graph of relative error ε_{static} versus relative density ρ_{rel} for a BCC unit cell employing both a fixed coefficient of 1.5 and an optimized coefficient. (b) Aggregated results showing the optimized penalty coefficient α_r^* across various studied lattice structures.

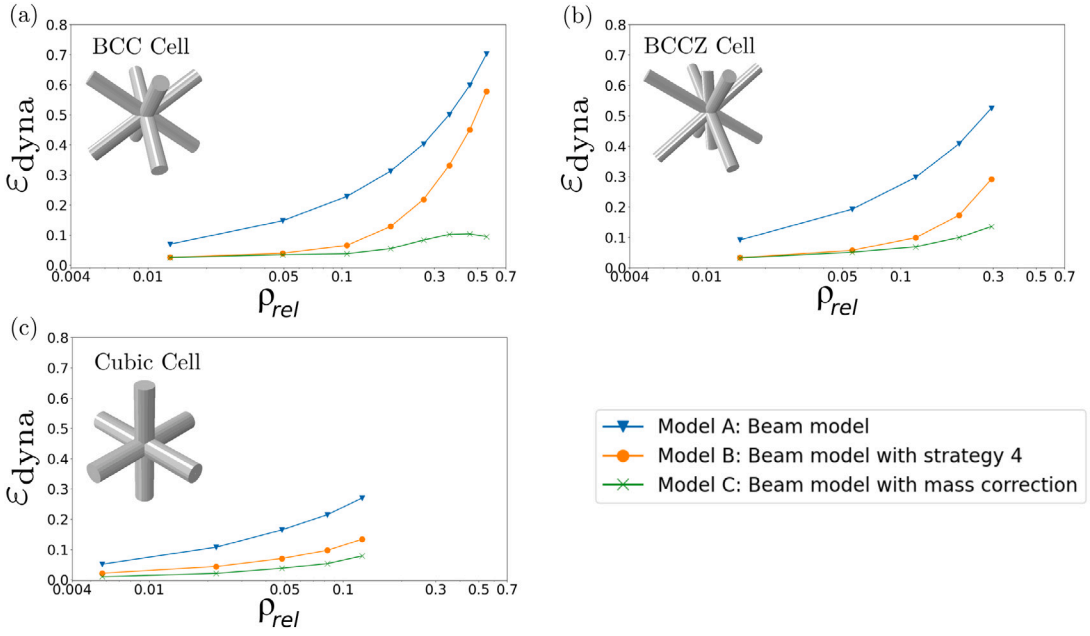

Fig. 9. Relative errors in frequency mode for (a) BCC, (b) BCCZ, and (c) Cubic cells across three modelization methodologies showing the impact of joint modifications and mass distribution on accuracy.

for each cell type is $\alpha_r = 1.496$, not far from $\alpha_r = 1.4$ as reported in existing literature (Smith et al., 2013; Labeas and Sunaric, 2010; Guo et al., 2020). Thus, based on our results, we suggest to set the penalty parameter as $\alpha_r = 1.5$. Interestingly, as shown in Fig. 8(a), such a fixed value leads to very similar results to the ones obtained with the optimal penalty parameters for the BCC cell. We also observed the same behavior for the other unit cells. Selecting l_{zone} as defined in Eq. (14) and $\alpha_r = 1.5$ leads to satisfactory results with significant improvements to the original non-penalized beam models as already highlighted in Fig. 7. The deviations between beam models with the identified penalty method and solid 3D models is about 10% at different relative densities for each unit cell: 0.3 for BCC, 0.25 for BCCZ and 0.1 for Cubic cell.

3.3. Evaluating added mass effects on the structural dynamics

As pointed out in Section 2.4, the material density in the penalized region might need to be adapted in order to recover appropriate structural dynamics. In order to investigate this point, we perform modal analyses over unit cells for which we compute the dynamic error ε_{dyna} as defined in Eq. (12). The number of computed modes is $N_{modes} = 20$. Those analyzes are done with the following beam models:

- Beam model without any modifications (referred to as Model A),

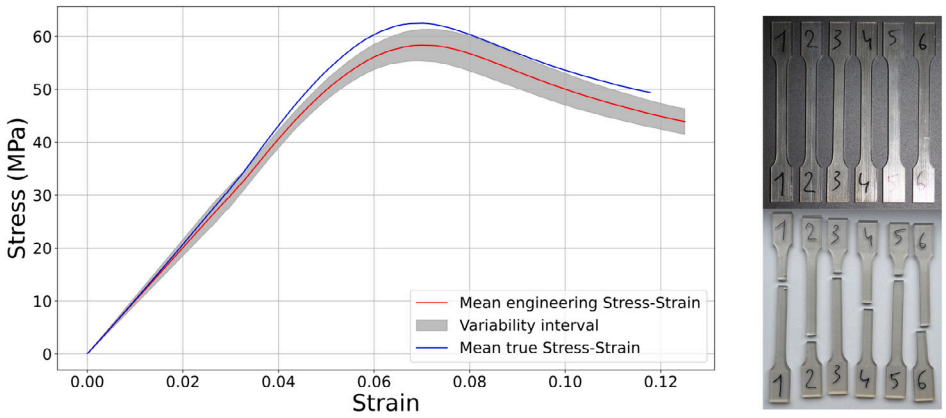

Fig. 10. Stress–strain response of VeroClear™ material fabricated using material jetting technology.

- Beam model employing Strategy 4 with a radius increase coefficient $\alpha_r = 1.5$ but no mass balance (referred to as Model B),
- Beam model employing Strategy 4, $\alpha_r = 1.5$, and mass correction, detailed below (referred to as Model C).

In Fig. 9 are compiled the results for BCC, BCCZ, and Cubic lattice geometries. Across all structures, a similar trend is observed for Model A: the relative error progressively increases with the relative density. This recurring trend highlights the essential need for modifications in beam joints to preserve accuracy. Model B reduces the natural frequency differences with the solid model at low relative density. However, this model exhibits a rapid escalation of the relative error as the relative density increases. This effect is attributable to, on one hand, the improvement of rigidity from the modifications at nodes, and on the other hand, the worsening of the mass repartition within the structure. Model C corrects this issue by re-establishing the mass distribution on the nodes. One can observe the large improvements obtained with this last model for all three lattice unit cells in Fig. 9. In conclusion, conducting dynamic simulations of lattice structures using FE beam models requires careful consideration of joint behavior and mass dispersion that arises from the application of stiffening correction.

4. Extension to nonlinear analyses and experimental comparison

In this section, we investigate whereas the obtained improvements with the selected penalty parameters over linear elastic simulations are also observed in the context of more advanced cases, and especially against experimental data.

4.1. Experimental framework

Material jetting AM is particularly beneficial for lattice structure production due to its high precision, essential for maintaining the intricate geometries and mechanical properties of lattice designs. It allows for unparalleled design freedom, enabling the creation of complex lattice configurations that are challenging with traditional manufacturing methods. Additionally, its multi-material capabilities and efficiency align well with sustainable manufacturing practices, making it a forward-thinking choice in modern engineering (Stankovic et al., 2015; Kreide et al., 2023). Test specimens were manufactured using a Stratasys Objet260 Connex3 printer, with VeroClear™ material. Experimental trials were conducted on a Lloyd LR 50K traction/compression machine. Quasi-static tensile tests were conducted on six specimens in accordance with the ISO 527-2 standard, and the results are compiled in Fig. 10. The material model has been established within the simulation software using an tabular dataset.

4.2. Uniaxial compression of an unit-cell made of elasto-plastic material

To assess the viability of our joint stiffening methodology in more complex cases, we investigate uniaxial compression tests over unit cells using the elasto-plastic material model obtained in Section 4.1. Geometric non-linearities are accounted for in the simulations, which allows for accurate modeling of large deformations and rotations (`NLGEOM` option in Abaqus). Several simulations are conducted. Indeed, three models are considered: a solid model considered as the reference model, a standard beam model without any joint stiffening methodology, and a beam model with our identified penalty method for the joint stiffening (a geometrical definition of the penalty region that takes into account the angles between the trusses, and a penalty coefficient $\alpha_r = 1.5$ that increases the radius of the cross-sections within these zones). BCC unit cell is studied with periodic boundary conditions across a relative density range of 0.05 to 0.46.

Fig. 11 illustrates the macroscopic stress–strain response from compression tests for each simulation methodology. The standard beam model consistently underpredicts the structural response across all densities, confirming again the need to formulate a beam modeling approach suitable for finite element simulations of lattice structures. The macro-stress is underestimated which indicates that the model is not stiff enough (as expected). The modified beam model, however, aligns closely with solid FE results for geometries with a relative density below 0.3. Beyond this threshold, the modified beam model tends to underestimate the macroscopic stress. These differences can likely be attributed to the mechanical behavior of the structures, which are not fully captured by the Timoshenko beam theory or the current treatment of plasticity within the beam formulation. It has been observed that plastic strain initiates earlier in the solid simulation compared to the beam model. Moreover, the modified beam model shows a relocation of the maximum stress at the edge of the stiffened region, altering the beam's behavior. This effect is more pronounced in lattice structures with high relative density.

Thus, the beam FE simulation domain is enhanced thanks to our stiffening modification methodology for elasto-plastic cases too. However, limitations are observed in the model's capability to simulate with low error for high relative densities. The relative error varies depending on the geometry of the lattice structure (see Section 3.1). Therefore, the proposed strategy must be used cautiously to avoid reaching excessively high errors. The stiffening methodology demonstrates satisfactory accuracy for lattice structures with a relative density below 0.3. Contrariwise, the methodology imposes no constraints on the geometries that can be treated, offering broad applicability in lattice structure simulations.

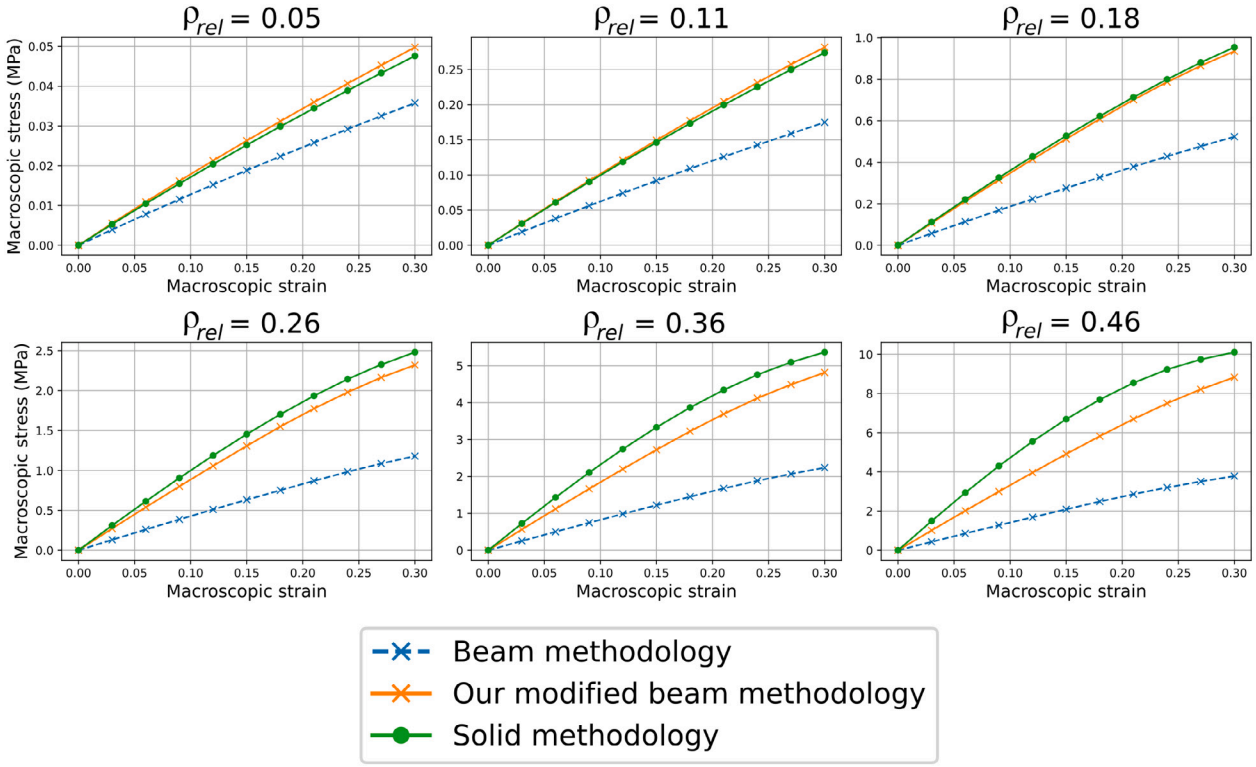

Fig. 11. Compression of BCC unit cell for beam, our beam modified and 3D solid model on a range of relative densities.

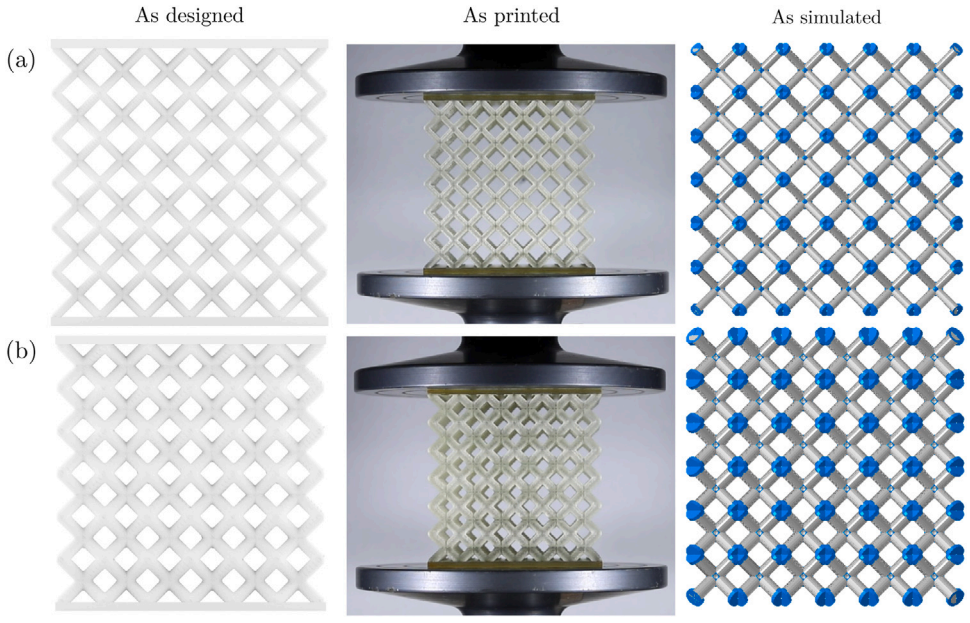

Fig. 12. As design, as printed and as simulated specimens of BCC lattice structure prepared for compression test (Beam radius: (a) 1 mm (b) 1.5 mm).

4.3. Experimental validation of the beam penalization methodology on 3D-printed BCC structures

Finally, to extend beyond numerical model comparisons (beam versus solid), we conducted experiments on lattice structures. The lattices are composed of 6-by-6-by-6 square cells with a side length of 10 mm (see Fig. 12). Two relative densities were chosen: one in the zone where the beam simulation method performs correctly (beam radius $R = 1.0$ mm $\Rightarrow \rho_{\text{rel}} = 0.169$) and one with a relative density too high (beam radius $R = 1.5$ mm $\Rightarrow \rho_{\text{rel}} = 0.345$). Quasi-static compression tests were conducted experimentally on these lattice structures, and similar tests were simulated using beam models without and with our joint stiffening approach, as well as solid FEM simulations.

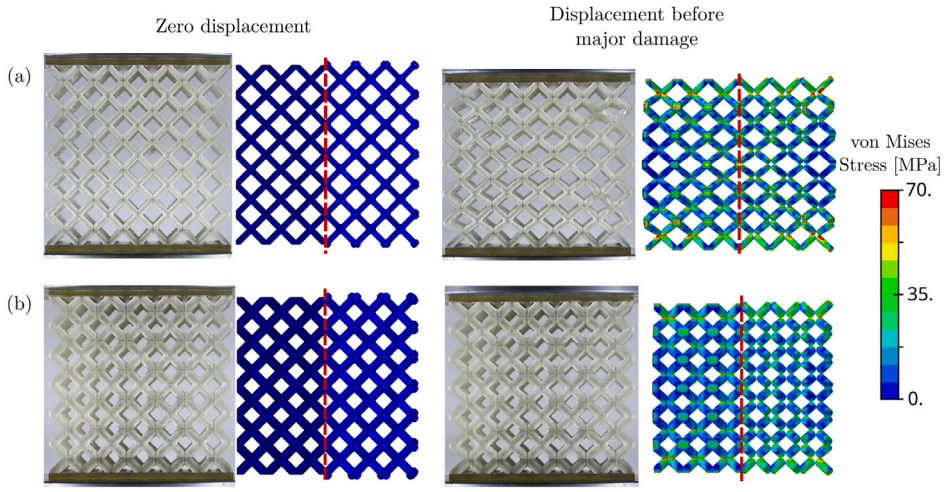

Fig. 13. Comparative visualization of 3D-printed specimens and simulation results (Solid FEM on the left of the red line and beam with optimal penalty parameters on the right) before major damage on experimental specimen (strain of (a) 0.07 and (b) 0.03) for BCC at relative density of (a) 0.17 and (b) 0.34.

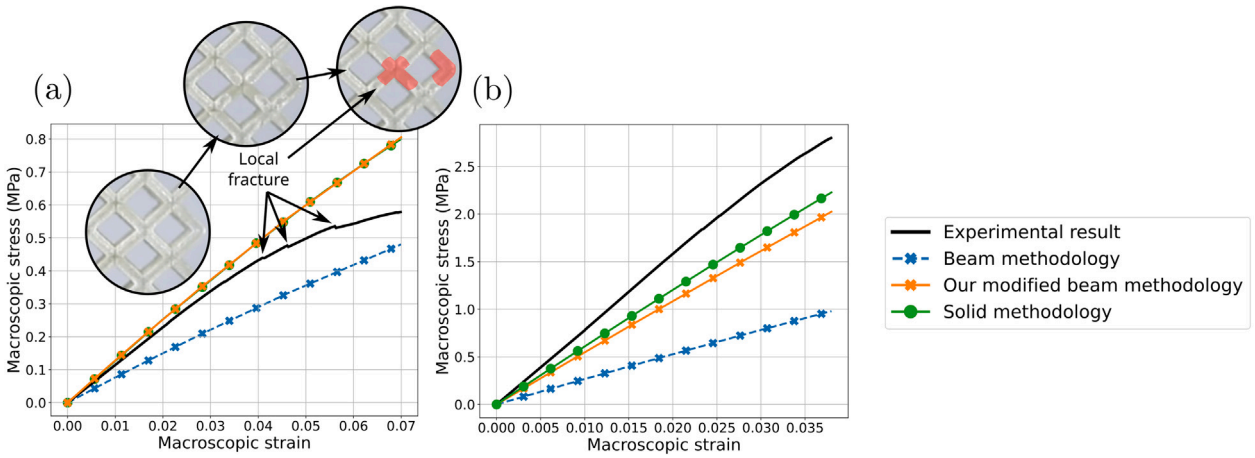

Fig. 14. Macroscopic stress–strain results: Experimental, Solid, Timoshenko and our modified beam methodology for BCC at relative densities of (a) 0.17 and (b) 0.34.

Fig. 13 illustrates the global correlation between the 3D-printed specimens during testing and the simulations, including both our modified beam methodology and the solid FEM simulation, before major damage to the experimental structure. In the case of full-scale lattice structure simulations, the number of elements in the mesh for solid models increases significantly, leading to a substantial computational burden. To manage this, we applied symmetry in the X,Y and Z planes to reduce the number of mesh elements. This constraint was not necessary for the beam models. Additionally, the simulation time for solid models is considerably longer, requiring over 14 h compared to just 2 min for the beam models on a standard laptop, excluding the time needed to generate the geometry. Complementary video 2 shows compression test of BCC lattice structures. The results exhibit a good concordance, underscoring the accuracy of the simulation in replicating experimental findings.

Fig. 14 synthesizes the macroscopic stress–strain data for each structural characterization method. The first point to note is that the differences between solid and beam models are consistent with those observed in unit-cell simulations (Section 4.2). For the BCC lattice structure with a 1 mm strut radius (Fig. 14(a)), our modified beam methodology accurately aligns with the experimental curve for small deformations, whereas the unmodified beam method underestimates the stiffness of the structure. At higher deformations, localized strut failures within the structure emerge, which are not accounted for in the material behavior simulations, leading to discrepancies. A more sophisticated material model would be required to accurately capture these phenomena; however, this is beyond the scope of the current article. In the case of the BCC structure with a 1.5 mm strut radius (Fig. 14(b)), the unmodified beam model performs very inadequately. The penalized beam model performs better, but the differences with the experimental results are not negligible. Interestingly, the solid model also fails to accurately predict the mechanical behavior of the structure, even if it performs a bit better. This is likely due to an insufficiently precise material model, resulting in these discrepancies.

5. Conclusion

In this paper, a novel methodology for simulating lattice structures using a FE beam model is proposed. By employing Timoshenko beam elements, this methodology significantly reduces the computational expenses commonly associated with solid FE simulations. This strategy

addresses the lake of rigidity at the nodes of the structure using three critical parameters:

$$l_{\text{zone}}(R,\gamma) = \frac{R}{\tan(\frac{\gamma}{2})}, \quad \alpha_{\text{r}} = 1.5, \quad \rho_{zone} = \frac{1}{V_{zone}}(m_{obj} - \rho V_{int}). \tag{18}$$

This methodology enables effective simulation of additively manufactured lattice structures effectively for linear, nonlinear, and dynamic behavior. It expands the domain of possible relative density for simulation through the rectification of the node rigidity via l_{zone} and α_{r}, as well as the mass balance via ρ_{zone}. However, limitations still exist on the domain of relative densities. The stiffening methodology demonstrates satisfactory accuracy for lattice structures with a relative density below 0.3. Experimental testing further validates the accuracy of the modified beam model in predicting the behavior of entire lattice structures.

The proposed simulation strategy is applicable not only to known lattice structures, but also to geometries with varying cellular dimensions or relative density gradients. The angles between the beams vary depending on the gradient function used, which is not considered in strategies using a constant l_{zone} length parameter. Functionally graded lattice structures are recognized for their superior performance across a broad spectrum of applications (Li et al., 2020; Maskery et al., 2018; Veloso et al., 2022), especially in terms of energy absorption (Chen et al., 2018b; Yang et al., 2016; Vangelatos et al., 2020). Furthermore, the development of a robust and efficient methodology enables the characterization of a wide range of lattice geometries exhibiting complex behaviors. Subsequently, large datasets can be leveraged to advance artificial intelligence (AI) models, deepening our understanding of the intricate behaviors exhibited by lattice structures. AI models can facilitate inverse design in practical applications, thereby accelerating advancements across numerous key sectors. This highlights that this strategy not only enhances the efficiency of lattice structure analysis but also opens up new possibilities for complex structural design and optimization in engineering applications.

CRediT authorship contribution statement

T. Cadart: Writing – original draft, Visualization, Software, Methodology, Investigation. **T. Hirschler:** Writing – review & editing, Validation, Supervision, Methodology, Investigation. **S. Bahi:** Writing – review & editing, Supervision. **S. Roth:** Writing – review & editing, Validation, Supervision. **F. Demoly:** Writing – review & editing, Supervision, Resources. **N. Lebaal:** Writing – review & editing, Supervision, Project administration, Funding acquisition.

Code availability

The code employed for generating results via Abaqus and for creating figures has been made available on GitHub.

Declaration of competing interest

The authors declare that they have no known competing financial interests or personal relationships that could have appeared to influence the work reported in this paper.

Acknowledgments

This work was partially supported by the IUF, a French government grant managed by the French Research Agency under the "France 2030" initiative and the DIADEM program (ANR-22-PEXD-0013, "ARTEMIS"), and Bourgogne-Franche-Comté Region.

Appendix A. Supplementary data

Supplementary material related to this article can be found online at https://doi.org/10.1016/j.ijsolstr.2024.113107.

Data availability

Data will be made available on request.

References

2024. VeroClear: a transparent 3D printing material. https://www.stratasys.com/en/materials/materials-catalog/polyjet-materials/veroclear/.

Alaimo, A., Del Prete, A., Mantegna, G., Orlando, C., Panella, F.W., Primo, T., Tumino, D., Vindigni, C.R., 2023. Modified beam modeling of powder bed fusion manufactured lattice structures. Int. J. Mech. Sci. 259, 108599. http://dx.doi.org/10.1016/j.ijmecsci.2023.108599.

Arabnejad, S., Pasini, D., 2013. Mechanical properties of lattice materials via asymptotic homogenization and comparison with alternative homogenization methods. Int. J. Mech. Sci. 77, 249–262. http://dx.doi.org/10.1016/j.ijmecsci.2013.10.003.

Atkinson, K.E., 1989. An Introduction to Numerical Analysis, 2. ed. Wiley, New York.

Brent, R.P., Watson, T.J., 1973. Algorithms for Minimization without Derivatives, George Forsythe Prentice-Hall.

Chen, D., Kitipornchai, S., Yang, J., 2018b. Dynamic response and energy absorption of functionally graded porous structures. Mater. Des. 140, 473–487. http://dx.doi.org/10.1016/j.matdes.2017.12.019.

Chen, Z., Wang, Z., Zhou, S., Shao, J., Wu, X., 2018a. Novel negative Poisson's ratio lattice structures with enhanced stiffness and energy absorption capacity. Materials 11 (7), 1095. http://dx.doi.org/10.3390/ma11071095.

Costa, M.R., Sohouli, A., Suleman, A., 2022. Multi-scale and multi-material topology optimization of gradient lattice structures using surrogate models. Compos. Struct. 289, 115402. http://dx.doi.org/10.1016/j.compstruct.2022.115402.

Dadashi, A., Rahimi, G., 2024. A comprehensive investigation of the lattice structure mechanical properties based on Schwarz primitive triply periodic minimal surface: Elastic modulus, yield strength, and maximum bearing force in the elastic region. Int. J. Solids Struct. 112776. http://dx.doi.org/10.1016/j.ijsolstr.2024.112776.

Dos Reis, F., Karathanasopoulos, N., 2022. Inverse metamaterial design combining genetic algorithms with asymptotic homogenization schemes. Int. J. Solids Struct. 250, 111702. http://dx.doi.org/10.1016/j.ijsolstr.2022.111702.

Dwyer, C.M., Carrillo, J.G., De la Peña, J.A.D., Santiago, C.C., MacDonald, E., Rhinehart, J., Williams, R.M., Burhop, M., Yelamanchi, B., Cortes, P., 2023. Impact performance of 3D printed spatially varying elastomeric lattices. Polymers 15 (5), 1178. http://dx.doi.org/10.3390/polym15051178.

Gao, Z., Wang, H., Letov, N., Zhao, Y.F., Zhang, X., Wu, Y., Leung, C.L.A., Wang, H., 2023. Data-driven design of biometric composite metamaterials with extremely recoverable and ultrahigh specific energy absorption. Composites B 251, 110468. http://dx.doi.org/10.1016/j.compositesb.2022.110468.

Gärtner, T., Fernández, M., Weeger, O., 2021. Nonlinear multiscale simulation of elastic beam lattices with anisotropic homogenized constitutive models based on artificial neural networks. Comput. Mech. 68 (5), 1111–1130. http://dx.doi.org/10.1007/s00466-021-02061-x.

Glaesener, R.N., Bastek, J.-H., Gonon, F., Kannan, V., Telgen, B., Spöttling, B., Steiner, S., Kochmann, D.M., 2021. Viscoelastic truss metamaterials as time-dependent generalized continua. J. Mech. Phys. Solids 156, 104569. http://dx.doi.org/10.1016/j.jmps.2021.104569.

Glaesener, R.N., Lestringant, C., Telgen, B., Kochmann, D.M., 2019. Continuum models for stretching- and bending-dominated periodic trusses undergoing finite deformations. Int. J. Solids Struct. 171, 117–134. http://dx.doi.org/10.1016/j.ijsolstr.2019.04.022.

Glaesener, R.N., Träff, E.A., Telgen, B., Canonica, R.M., Kochmann, D.M., 2020. Continuum representation of nonlinear three-dimensional periodic truss networks by on-the-fly homogenization. Int. J. Solids Struct. 206, 101–113. http://dx.doi.org/10.1016/j.ijsolstr.2020.08.013.

Gümrük, R., Mines, R.A.W., 2013. Compressive behaviour of stainless steel micro-lattice structures. Int. J. Mech. Sci. 68, 125–139. http://dx.doi.org/10.1016/j.ijmecsci.2013.01.006.

Guo, H., Takezawa, A., Honda, M., Kawamura, C., Kitamura, M., 2020. Finite element simulation of the compressive response of additively manufactured lattice structures with large diameters. Comput. Mater. Sci. 175, 109610. http://dx.doi.org/10.1016/j.commatsci.2020.109610.

Hajjari, M., Jafari Nedoushan, R., Dastan, T., Sheikhzadeh, M., Yu, W.-R., 2021. Lightweight weft-knitted tubular lattice composite for energy absorption applications: An experimental and numerical study. Int. J. Solids Struct. 213, 77–92. http://dx.doi.org/10.1016/j.ijsolstr.2020.12.017.

Hassani, B., Hinton, E., 1998. A review of homogenization and topology optimization I—Homogenization theory for media with periodic structure. Comput. Struct. 69 (6), 707–717. http://dx.doi.org/10.1016/S0045-7949(98)00131-X.

Helou, M., Kara, S., 2018. Design, analysis and manufacturing of lattice structures: An overview. Int. J. Comput. Integr. Manuf. 31 (3), 243–261. http://dx.doi.org/10.1080/0951192X.2017.1407456.

Henyš, P., Č.apek, L., Březina, J., 2019. Comparison of current methods for implementing periodic boundary conditions in multi-scale homogenisation. Eur. J. Mech. A Solids 78, 103825. http://dx.doi.org/10.1016/j.euromechsol.2019.103825.

Hirschler, T., Antolin, P., Buffa, A., 2022. Fast and multiscale formation of isogeometric matrices of microstructured geometric models. Comput. Mech. 69 (2), 439–466. http://dx.doi.org/10.1007/s00466-021-02098-y.

Hirschler, T., Bouclier, R., Antolin, P., Buffa, A., 2024. Reduced order modeling based inexact FETI-DP solver for lattice structures. Internat. J. Numer. Methods Engrg. 125 (8), e7419. http://dx.doi.org/10.1002/nme.7419.

Kreide, C., Koricho, E., Kardel, K., 2023. Energy absorption of 3D printed multi-material elastic lattice structures. Prog. Addit. Manuf. http://dx.doi.org/10.1007/s40964-023-00529-1.

Labeas, G.N., Sunaric, M.M., 2010. Investigation on the static response and failure process of metallic open lattice cellular structures. Strain 46 (2), 195–204. http://dx.doi.org/10.1111/j.1475-1305.2008.00498.x.

Li, Y., Feng, Z., Hao, L., Huang, L., Xin, C., Wang, Y., Bilotti, E., Essa, K., Zhang, H., Li, Z., Yan, F., Peijs, T., 2020. A review on functionally graded materials and structures via additive manufacturing: From multi-scale design to versatile functional properties. Adv. Mater. Technol. 5 (6), 1900981. http://dx.doi.org/10.1002/admt.201900981.

Ling, C., Cernicchi, A., Gilchrist, M.D., Cardiff, P., 2019. Mechanical behaviour of additively-manufactured polymeric octet-truss lattice structures under quasi-static and dynamic compressive loading. Mater. Des. 162, 106–118. http://dx.doi.org/10.1016/j.matdes.2018.11.035.

Liu, X., Gao, L., Xiao, M., Zhang, Y., 2022. Kriging-assisted design of functionally graded cellular structures with smoothly-varying lattice unit cells. Comput. Methods Appl. Mech. Engrg. 390, 114466. http://dx.doi.org/10.1016/j.cma.2021.114466.

Liu, J., Guo, K., Sun, J., Sun, Q., Wang, L., Li, H., 2021a. Compressive behavior and vibration-damping properties of porous Ti-6Al-4V alloy manufactured by laser powder bed fusion. J. Manuf. Process. 66, 1–10. http://dx.doi.org/10.1016/j.jmapro.2021.03.060.

Liu, F., Wang, L., Jin, D., Liu, X., Lu, P., 2021b. Equivalent beam model for spatial repetitive lattice structures with hysteretic nonlinear joints. Int. J. Mech. Sci. 200, 106449. http://dx.doi.org/10.1016/j.ijmecsci.2021.106449.

Lozanovski, B., Downing, D., Tino, R., du Plessis, A., Tran, P., Jakeman, J., Shidid, D., Emmelmann, C., Qian, M., Choong, P., Brandt, M., Leary, M., 2020a. Non-destructive simulation of node defects in additively manufactured lattice structures. Addit. Manuf. 36, 101593. http://dx.doi.org/10.1016/j.addma.2020.101593.

Lozanovski, B., Downing, D., Tran, P., Shidid, D., Qian, M., Choong, P., Brandt, M., Leary, M., 2020b. A Monte Carlo simulation-based approach to realistic modelling of additively manufactured lattice structures. Addit. Manuf. 32, 101092. http://dx.doi.org/10.1016/j.addma.2020.101092.

Lumpe, T.S., Stankovic, T., 2021. Exploring the property space of periodic cellular structures based on crystal networks. Proc. Natl. Acad. Sci. USA 118 (7), e2003504118. http://dx.doi.org/10.1073/pnas.2003504118.

Luxner, M.H., Stampfl, J., Pettermann, H.E., 2005. Finite element modeling concepts and linear analyses of 3D regular open cell structures. J. Mater. Sci. 40 (22), 5859–5866. http://dx.doi.org/10.1007/s10853-005-5020-y.

Maskery, I., Aremu, A.O., Parry, L., Wildman, R.D., Tuck, C.J., Ashcroft, I.A., 2018. Effective design and simulation of surface-based lattice structures featuring volume fraction and cell type grading. Mater. Des. 155, 220–232. http://dx.doi.org/10.1016/j.matdes.2018.05.058.

McDonnell, B., O'Hara, E.M., Harrison, N.M., 2024. Simulation-driven-design of metal lattice structures for a target stress–strain curve. Mater. Des. 237, 112543. http://dx.doi.org/10.1016/j.matdes.2023.112543.

Meng, L., Qiu, X., Gao, T., Li, Z., Zhang, W., 2020. An inverse approach to the accurate modelling of 3D-printed sandwich panels with lattice core using beams of variable cross-section. Compos. Struct. 247, 112363. http://dx.doi.org/10.1016/j.compstruct.2020.112363.

Monaldo, E., Marfia, S., 2021. Multiscale technique for the analysis of 3D-printed materials. Int. J. Solids Struct. 232, 111173. http://dx.doi.org/10.1016/j.ijsolstr.2021.111173.

Musenich, L., Stagni, A., Libonati, F., 2023. Hierarchical bioinspired architected materials and structures. Extreme Mech. Lett. 58, 101945. http://dx.doi.org/10.1016/j.eml.2022.101945.

Omairey, S.L., Dunning, P.D., Sriramula, S., 2019. Development of an ABAQUS plugin tool for periodic RVE homogenisation. Eng. Comput. 35 (2), 567–577. http://dx.doi.org/10.1007/s00366-018-0616-4.

Pilkey, W.D., 2002. Analysis and Design of Elastic Beams: Computational Methods, first ed. Wiley, http://dx.doi.org/10.1002/9780470172667.

Raju, K., Tay, T., Tan, V.B.C., 2021. A review of the FE2 method for composites. Multiscale Multidiscip. Model. Exp. Des. 4, http://dx.doi.org/10.1007/s41939-020-00087-x.

Ross, E., Hambleton, D., 2021. Using Graph Neural Networks to approximate mechanical response on 3D lattice structures. Proc AAG2020-Advances Archit. Geom. 24, 466–485.

Scalzo, F., Totis, G., Vaglio, E., Sortino, M., 2021. Experimental study on the high-damping properties of metallic lattice structures obtained from SLM. Precis. Eng. 71, 63–77. http://dx.doi.org/10.1016/j.precisioneng.2021.02.010.

Schwahofer, O., Büttner, S., Colin, D., Drechsler, K., 2023. Tailored elastic properties of beam-based lattice unit structures. Int. J. Mech. Mater. Des. http://dx.doi.org/10.1007/s10999-023-09659-4.

Smith, M., Guan, Z., Cantwell, W.J., 2013. Finite element modelling of the compressive response of lattice structures manufactured using the selective laser melting technique. Int. J. Mech. Sci. 67, 28–41. http://dx.doi.org/10.1016/j.ijmecsci.2012.12.004.

Somnic, J., Jo, B.W., 2022a. Homogenization methods of lattice materials. Encyclopedia 2 (2), 1091–1102. http://dx.doi.org/10.3390/encyclopedia2020072.

Somnic, J., Jo, B.W., 2022b. Status and challenges in Homogenization Methods for lattice materials. Materials 15 (2), 605. http://dx.doi.org/10.3390/ma15020605.

Stankovic, T., Mueller, J., Egan, P., Shea, K., 2015. Optimization of additively manufactured multi-material lattice structures using generalized optimality criteria. In: Volume 1A: 35th Computers and Information in Engineering Conference. American Society of Mechanical Engineers, Boston, Massachusetts, USA, http://dx.doi.org/10.1115/DETC2015-47403, V01AT02A026.

Tahmasebimoradi, A., Mang, C., Lorang, X., 2021. A numerical hybrid finite element model for lattice structures using 3d/beam elements. In: ASME 2021 International Mechanical Engineering Congress and Exposition. American Society of Mechanical Engineers, Virtuel, France, http://dx.doi.org/10.1115/IMECE2021-69119.

Terriault, P., Brailovski, V., 2018. Modeling and simulation of large, conformal, porosity-graded and lightweight lattice structures made by additive manufacturing. Finite Elem. Anal. Des. 138, 1–11. http://dx.doi.org/10.1016/j.finel.2017.09.005.

Vangelatos, Z., Komvopoulos, K., Spanos, J., Farsari, M., Grigoropoulos, C., 2020. Anisotropic and curved lattice members enhance the structural integrity and mechanical performance of architected metamaterials. Int. J. Solids Struct. 193–194, 287–301. http://dx.doi.org/10.1016/j.ijsolstr.2020.02.023.

Veloso, F., Gomes-Fonseca, J., Morais, P., Correia-Pinto, J., Pinho, A.C., Vilaça, J.L., 2022. Overview of methods and software for the design of functionally graded lattice structures. Adv. Eng. Mater. 24 (11), 2200483. http://dx.doi.org/10.1002/adem.202200483.

Wang, J., Zhu, J., Liu, T., Wang, Y., Zhou, H., Zhang, W.-H., 2023. Topology optimization of gradient lattice structure under harmonic load based on multiscale finite element method. Struct. Multidiscip. Optim. 66 (9), 202. http://dx.doi.org/10.1007/s00158-023-03652-3.

Weeger, O., Boddeti, N., Yeung, S.K., Kaijima, S., Dunn, M.L., 2019. Digital design and nonlinear simulation for additive manufacturing of soft lattice structures. Addit. Manuf. 25, 39–49. http://dx.doi.org/10.1016/j.addma.2018.11.003.

Weeger, O., Valizadeh, I., Mistry, Y., Bhate, D., 2023. Inelastic finite deformation beam modeling, simulation, and validation of additively manufactured lattice structures. Addit. Manuf. Lett. 4, 100111. http://dx.doi.org/10.1016/j.addlet.2022.100111.

Wu, Y., Fang, J., Wu, C., Li, C., Sun, G., Li, Q., 2023. Additively manufactured materials and structures: A state-of-the-art review on their mechanical characteristics and energy absorption. Int. J. Mech. Sci. 246, 108102. http://dx.doi.org/10.1016/j.ijmecsci.2023.108102.

Xiao, L., Song, W., Xu, X., 2020. Experimental study on the collapse behavior of graded Ti-6Al-4V micro-lattice structures printed by selective laser melting under high speed impact. Thin-Walled Struct. 155, 106970. http://dx.doi.org/10.1016/j.tws.2020.106970.

Yang, K., Hu, X., Pan, F., Qiao, C., Ding, B., Hu, L., Hu, X., He, Z., Chen, Y., 2023. An on-demand tunable energy absorption system to resolve multi-directional impacts. Int. J. Solids Struct. 271–272, 112257. http://dx.doi.org/10.1016/j.ijsolstr.2023.112257.

Yang, W., Yue, Z., Xu, B., 2016. A hybrid elastomeric foam-core/solid-shell spherical structure for enhanced energy absorption performance. Int. J. Solids Struct. 92–93, 17–28. http://dx.doi.org/10.1016/j.ijsolstr.2016.05.001.

Yin, H., Zhang, W., Zhu, L., Meng, F., Liu, J., Wen, G., 2023. Review on lattice structures for energy absorption properties. Compos. Struct. 304, 116397. http://dx.doi.org/10.1016/j.compstruct.2022.116397.

Zhang, N., Ma, X., Chang, Y., Tian, X., 2024. A lattice structure with adjustable mechanical behavior constructed by rotating triangles translated out of plane and splicing each other. Int. J. Solids Struct. 292, 112740. http://dx.doi.org/10.1016/j.ijsolstr.2024.112740.

Zhang, H.-w., Wu, J., Fu, Z., 2010. Extended multiscale finite element method for mechanical analysis of periodic lattice truss materials. Int. J. Multiscale Comput. Eng. 8, 597–613. http://dx.doi.org/10.1615/IntJMultCompEng.v8.i6.40.

Zheng, L., Karapiperis, K., Kumar, S., Kochmann, D.M., 2023. Unifying the design space and optimizing linear and nonlinear truss metamaterials by generative modeling. Nature Commun. 14 (1), 7563. http://dx.doi.org/10.1038/s41467-023-42068-x.